Progress In Electromagnetics Research M, Vol. 109, 75–88, 2022

Influence of Magnetic Remanence and Coercive Force on the Electromagnetic Output of Permanent Magnet Machine

Stephen E. Oti[1] and Chukwuemeka C. Awah[2, *]

Abstract—The impact of permanent magnet (PM) properties such as magnet remanence and coercive force or coercivity on the electromagnetic output of flux-switching permanent magnet machine having C-core stator topology is presented and compared in this work. A two-dimensional finite-element analysis (2D-FEA) approach is implemented using ANSYS-MAXWELL software package. Three-dimensional (3D) FEA calculations are also conducted, in order to realize more accurate results, and its results are compared with the 2D-FEA predicted results. The investigated machine elements are: airgap flux-density, torque ripple, total harmonic distortion (THD) of the voltage, cogging torque, unbalanced magnetic pull (UMP) or force, winding inductances, direct- and quadrature-axis flux, electromotive force, and output torque. The analyses show that undesirable qualities such as large amount of cogging torque and UMP are predominant in the machine having rare-earth magnets, i.e., neodymium and samarium-cobalt, although they have larger flux linkage and superior average torque compared to its non-rare-earth magnet equivalents, i.e., the ferrite- and alnico-made machines. Moreover, the alnico- and ferrite-made machines exhibit larger winding inductance values, and consequently lower saturation withstand capability, though with better field-weakening capability. Further, the predicted efficiencies of the compared machine types having alnico, ferrite, neodymium and samarium materials, at rated current and speed conditions are: 79.8%, 75.76%, 87.22%, and 86.58%, respectively. More so, the generated electromagnetic output power of the compared machine types at the operating base speed is: 206.57 Watts, 186.57 Watts, 449.67 Watts, and 396.40 Watts, respectively. The investigated machine is suitable for high torque in-wheel direct-drive applications.

1. INTRODUCTION

The effect of permanent magnet materials on the overall performance of an electric machine cannot be underestimated. Therefore, the present study undertakes the consideration of some magnetic properties such as remanence, coercive force (coercivity), and energy product of a given flux-switching permanent magnet machine with special attention to different types of magnets. The used magnetic materials in this study are: I. Rare-earth magnets, i.e., Neodymium-iron-boron (NdFeB), grade N52 and Samarium-cobalt (SmCo), grade S24. II. Non-rare-earth magnets, i.e., Alnico, grade A500 and Ferrite, grade F5. The stator and rotor units are made of low carbon silicon steel, i.e., M330-35A. The investigated machine 2D- and 3D-models are depicted in Figs. 1(a) and (b), while its corresponding 3D-FEA mesh and no-load flux density outlines are shown in Figs. 1(c) and (d), respectively.

The cost of rare-earth magnetic materials such as neodymium and samarium-cobalt is high and thus limits the commercialization of high-energy permanent magnet (PM) machines, as noted in [1]. Despite the very exorbitant price of SmCo-made magnetic machines relative to the NdFeB types, SmCo-made magnetic machines have good thermal management and strength compared to the neodymium magnetic

Received 27 January 2022, Accepted 14 March 2022, Scheduled 28 March 2022
* Corresponding author: Chukwuemeka C. Awah (ccawah@ieee.org).
[1] Department of Electrical Engineering, University of Nigeria, Nsukka, Nigeria. [2] Department of Electrical and Electronic Engineering, Michael Okpara University of Agriculture, Umudike, Nigeria.

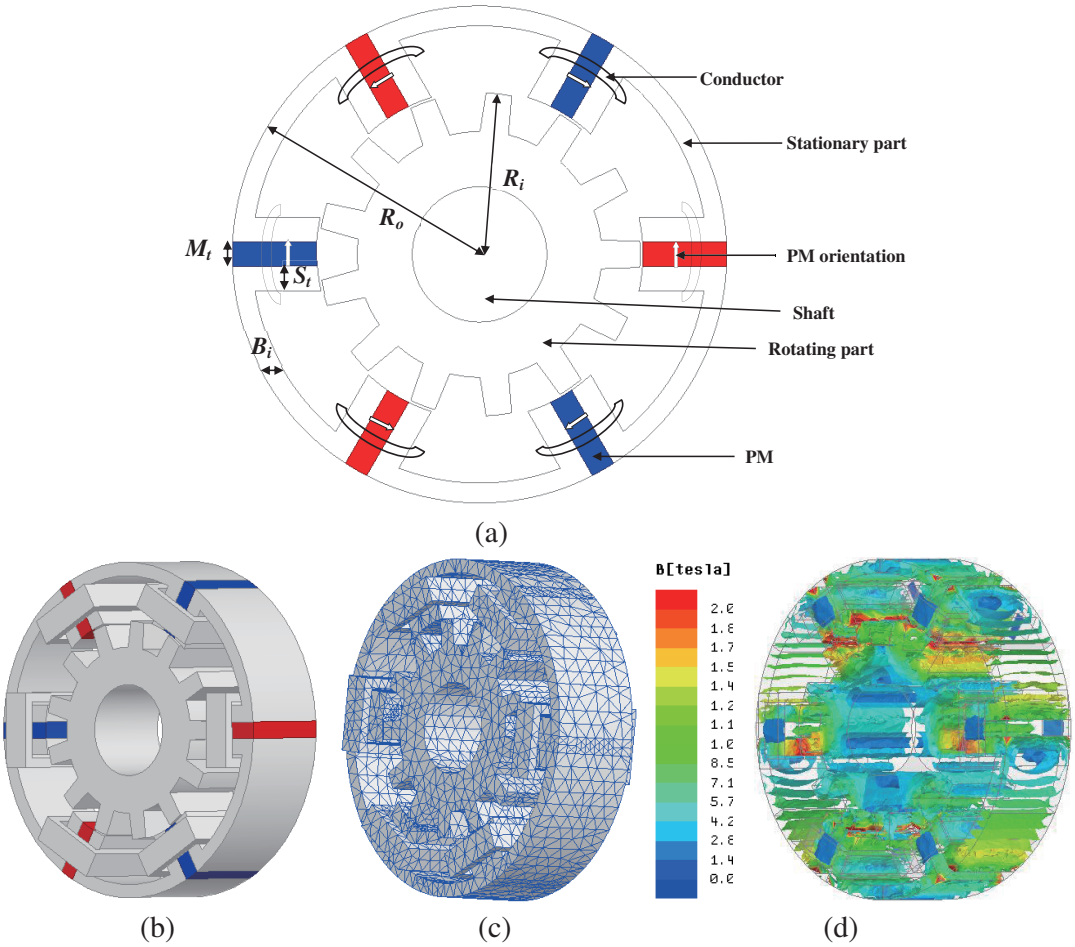

Figure 1. Schematic diagrams of the investigated machine model. (a) 2D FEA model [7]. (b) 3D FEA model. (c) 3D FEA mesh. (d) 3D FEA flux density.

machines, with additional ability to sustain corrosion effect, as highlighted in [2]. The market price of the magnets is listed in Table 1 of the current study, for clarity. Therefore, efforts toward developing high-output machines with little or no rare-earth magnet are on the increase as evidenced in [3], though with increased machine axial length compared to the rare-earth ones. Secondly, a combination of the duo magnet sets, i.e., hybrid integration of rare-earth and non-rare-earth PMs, is also widely researched [4]. Such hybrid systems could enhance the anti-demagnetization proficiency of the machine [5], without compromising its economic target. Moreover, implemented winding configuration and excitation plan play important roles on the overall output of hybrid-excited PM machines according to the report in [6]. Consequently, parallel excitation strategy coupled with flux-concentration technique is recommended for high torque-density, although a combination of series and parallel excitation arrangements would result in an improved demagnetization tolerance at the expense of some torque. The investigated machine model is a flux-switching permanent magnet machine proposed in [7], however with only one type of magnet.

Normally, permanent magnet machine having ferrite magnet could produce competitive efficiency and comparable power with that having rare-earth magnets, but usually with a direct consequence of greater machine active length, i.e., about five times the usual active length may be required. However, this may also go with a drawback of critical speed reduction as stated in [8]. In addendum, it will lead to increased overall machine weight and enlarged magnetic material volume. Nevertheless, it is still cheaper than the cost of producing the same machine with high-energy rare-earth magnetic materials. Note that by employing a suitable optimization approach in addition to the use of more ferrite materials,

a ferrite-made machine driven at low load below the rated current condition could enhance the machine's power factor as given in [9].

Further, the electromagnetic performance of PM machine utilizing ferrite magnets could be significantly improved by maximizing its torque components, i.e., the reluctance and magnetic torques via appropriate rotor geometric design and optimization technique, as detailed in [10]. Although it is well known that PM machine is made of non-rare-earth magnets, the ferrite ones are mainly liable to higher demagnetization danger. Thus, the ferrite-made electric machines are more likely to demagnetize irreversibly than their neodymium-iron-boron equivalent ones, owing to the small coercivity level of the former, as proved in [11]. In addition, the potential of a given magnet to demagnetize would also depend on its size; hence, the larger the volume of the used magnetic material is, the safer for the machine, albeit, at an increased cost penalty. Nevertheless, demagnetization weakness of such PMs could also be ameliorated by modification of the machine's physical geometry through optimization [12]. Furthermore, the demagnetization flaw of any given PM machine is worsened when its direct-axis inductance is larger than the corresponding quadrature-axis inductance, as pointed out in [13], though such a machine may be a promising candidate in terms of good field-weakening capability. Therefore, there is a need for compromise during the initial design and optimization stage. More so, a comparative study between the uses of samarium-cobalt and ferrite magnets given in [14] shows that an electric machine that is furnished with low-energy ferrite material can yield a similar electromagnetic output to that having samarium-cobalt by manipulating its magnetic-loading in favor of the electric loading. Overall, an enhanced number of turns per phase, a reduced motor speed, and enlarged machine stack-length are the consequences of using ferrite material to achieve a comparable result to the rare-earth magnetic counterparts. However, the very high cost of samarium-cobalt material should not be overlooked. It is worth noting that the studies in [15] show that rare-earth magnets exhibit lots of competitive advantages over its non-rare-earth counterparts.

Additionally, non-rare-earth magnetic materials such as alnico with relatively high coercivity skill are improved for cost effectiveness and good performance to compete with the existing rare-earth ones, though significant work is still underway to enhance the remanence ability of such alnico magnets, as pointed out in [16]. Again, comparable efficiency and improved output per magnet usage could be obtained from an electrical machine that has ferrite magnetic materials compared to the ones having rare-earth magnets, albeit, with poorer mechanical strength, and again with higher weakness to demagnetization effects, as highlighted in [17]. Nevertheless, demagnetization drawbacks in an electrical machine could be minimized by series-combination of rare-earth magnetic material and a low energy product magnet, such as alnico for possible continuous re-magnetization of the alnico magnet, owing to an arrangement where both magnets would have two independent magnetic flux routes, as demonstrated in [18].

Clearly, the flux-density contours displayed in Fig. 2 show that the concentration of flux is most effective around the stator-tooth and rotor-tooth tips which are near the airgap areas. The predicted finite element analysis (FEA) magnetic remanence and its corresponding coercive force or coercivity around the airgap of the analyzed machine are displayed in Fig. 3. It is obvious that the intensity of the linking flux coupled with their analogous coercive force around the airgap of the compared machine is more pronounced and evident in the rare-earth magnetic materials due to their intrinsic high magnetic remanence and coercive force (coercivity). More so, the stator yoke or back-iron of the non-rare-earth magnets saturates faster, especially at high current-density loadings, due to the higher level of armature reaction it experiences at such condition than the rare-earth ones, bearing in mind the small overall size of the analyzed machine. The basic machine elements as well as the machine's dimensions and values are detailed in Table 1.

Permanent magnet (PM) remanence and PM coercive force (coercivity) are the major magnetic material properties of a given magnet, which would determine its resultant energy product level. Thus, these two magnetic properties are presented side by side in Fig. 3, with different magnitudes and units. More so, the simulation is carried out in one electric revolution as the rotor rotates at different angular positions. Note also that the investigated machine is a rotating machine, thus the resulting amplitudes of PM magnetic properties would depend upon the specific angular position of the rotor at a given time.

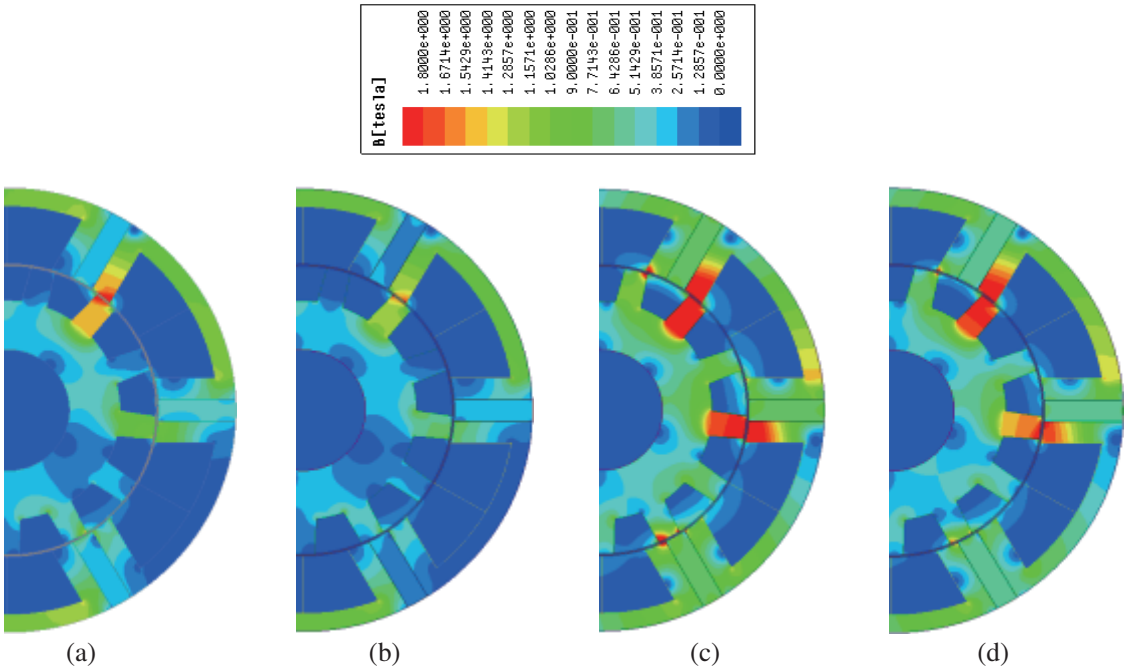

Figure 2. Flux density at 5 A/mm^2. (a) alnico, (b) ferrite, (c) neodymium, (d) samarium.

Table 1. Parameters and units of the compared machine having different magnets.

Parameter	**Value**			
Stator poles, P_s	6			
Rotor poles, P_r	13			
Machine outer radius, R_o (mm)	45			
Rotor outer radius, R_i (mm)	29.16			
Magnet thickness, M_t (mm)	4.45			
Phase number of turns, N_t	72			
Material type	**Alnico**	**Ferrite**	**Neodymium**	**Samarium Cobalt**
PM remanence, B_r, (T)	1.16	0.4	1.47	1.05
Coercivity, H, (kA/m)	230.75	303.15	1063.4	795.77
Electromagnetic power at base speed, (W)	206.57	186.57	449.67	396.40
Efficiency at rated speed (%)	79.83	75.76	87.22	86.58
Energy product, BH_{m}, (MGOe)	4.4	3.7	53	25.8
Cost, (\$/pound weight)	20	2	35	70
Flux-weakening factor, F_{wp}	2.57	2.76	0.60	0.87
D-axis inductance, L_D, (mH)	1.0571	0.8744	0.4215	0.5766
Q-axis inductance L_Q, (mH)	0.9679	0.8460	0.5004	0.6291
L_Q/L_D, saliency ratio	0.9157	0.9676	1.1872	1.0909

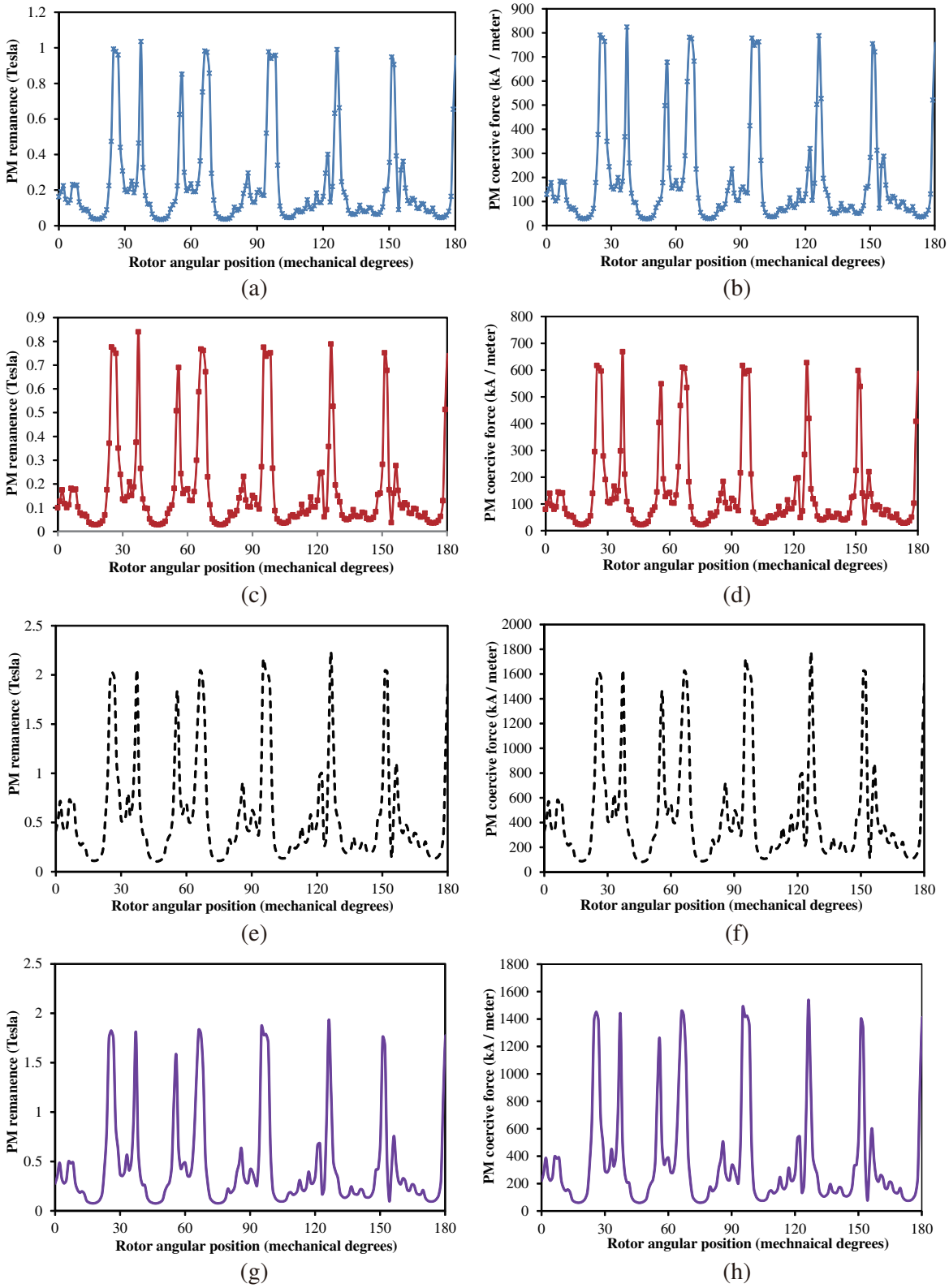

Figure 3. Magnet remanence and corresponding coercive force, 2D FEA, (a) alnico, (b) alnico, (c) ferrite, (d) ferrite, (e) neodymium, (f) neodymium, (g) samarium, (h) samarium.

2. TORQUE AND VOLTAGE CHARACTERISTICS

The variation of torque ripple and total harmonic distortion (THD) of the voltage is presented in Figs. 4(a) and (b). Initially, the predicted torque ripple tends to decrease from the very low load or no-load condition due to the cogging torque effect before rising in response to the increasing load current. Generally, the compared torque ripple outlines show different trends particularly for the ferrite-made machine. Meanwhile, it is rightly emphasized in [19] that the total harmonic distortion and torque ripple are not necessarily associated together, since every machine has a specific collapse limit owing to the machine's peculiar to resist electromagnetic overload caused by armature reaction. Over the whole range of electric loading, it is seen that the non-rare-earth magnetic materials take the lead in terms of higher amount of THD, which suggests higher voltage harmonic characteristics. Thus, such devices would not be easily amenable to electric machine control purposes relative to their rare-earth counterparts.

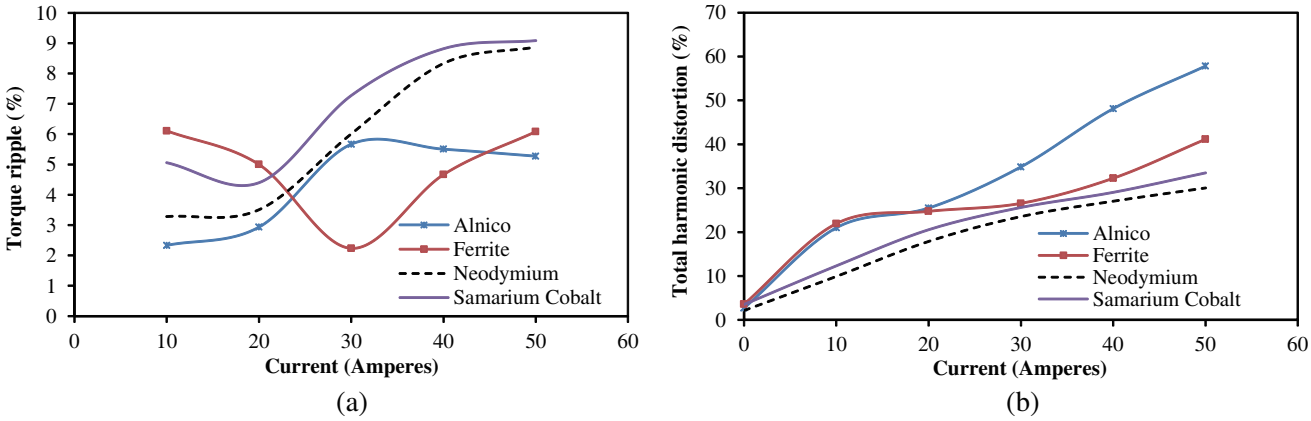

Figure 4. 2D FEA comparison of torque ripple and total harmonic distortion, (a) torque ripple versus current, (b) THD versus current.

The computed torque ripple equation is given in Eq. (1). Similarly, the predicted total harmonic distortion of the voltage is computed using Eq. (2).

$$T_r = \frac{T_{mx} - T_{mn}}{T_{av}} \tag{1}$$

where T_r is the torque ripple quantity, T_{mx} the maximum torque, T_{mn} the minimum torque, and T_{av} the average torque.

$$THD = \frac{\sum_{n=2}^{n} \sqrt{(V_2^2 + V_3^2 + \ldots + V_n^2)}}{V_1} \tag{2}$$

where V_1 is the fundamental harmonic order of the induced-voltage, and n is the nth order of harmonics.

Additionally, it is worth noting that the alnico-based magnetic machine produces the lowest amount of cogging torque as shown in Fig. 5, which is an attractive machine quality. The cogging torque waveforms with their respective fast Fourier transform (FFT) spectra are shown in Fig. 5. Essentially, it is seen that the cogging torque waveforms and magnitudes are larger in the rare-earth PM machines than in its equivalent non-rare-earth types. Further, the number of cogging torque cycles, CT_{cycle}, in one electric period is given in Eq. (3). For example, the highest common factor (HCF) between 6 stator poles and 13 rotor poles is 1; therefore, 6 divided by 1 gives 6 cycles, as obtained in Fig. 5. This concept about cogging torque cycle also reflects in the harmonic spectra shown in Fig. 5(b), where the largest predicted FFT amplitude of cogging torques is recorded in the dominant sixth order. The electromagnetic torque, T, induced-electromotive force, E, supplied phase currents, I_A, I_B, I_C, and

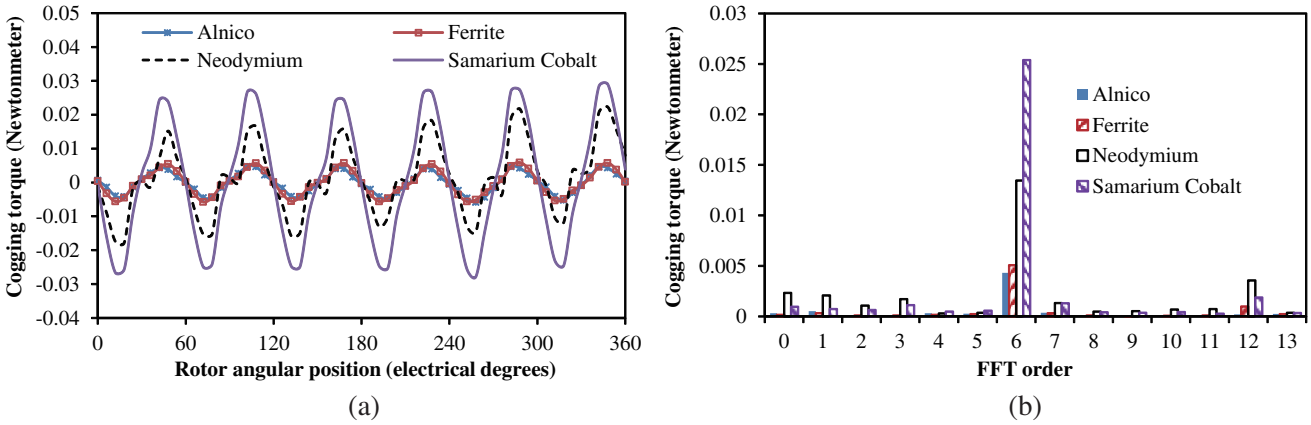

Figure 5. 2D FEA comparison of cogging torque, (a) waveforms, (b) harmonic order.

machine's rotational speed, ω, are related in Eq. (4).

$$CT_{cycle} = \frac{P_s}{HCF(P_s, P_r)} \tag{3}$$

$$T\omega = E_A I_A + E_B I_B + E_C I_C \tag{4}$$

Figure 6 depicts the variation of direct (D)-axis and quadrature (Q)-axis flux with quadrature-axis current, as well as the induced-electromotive force FFT amplitudes as a function of rotor speed. It is

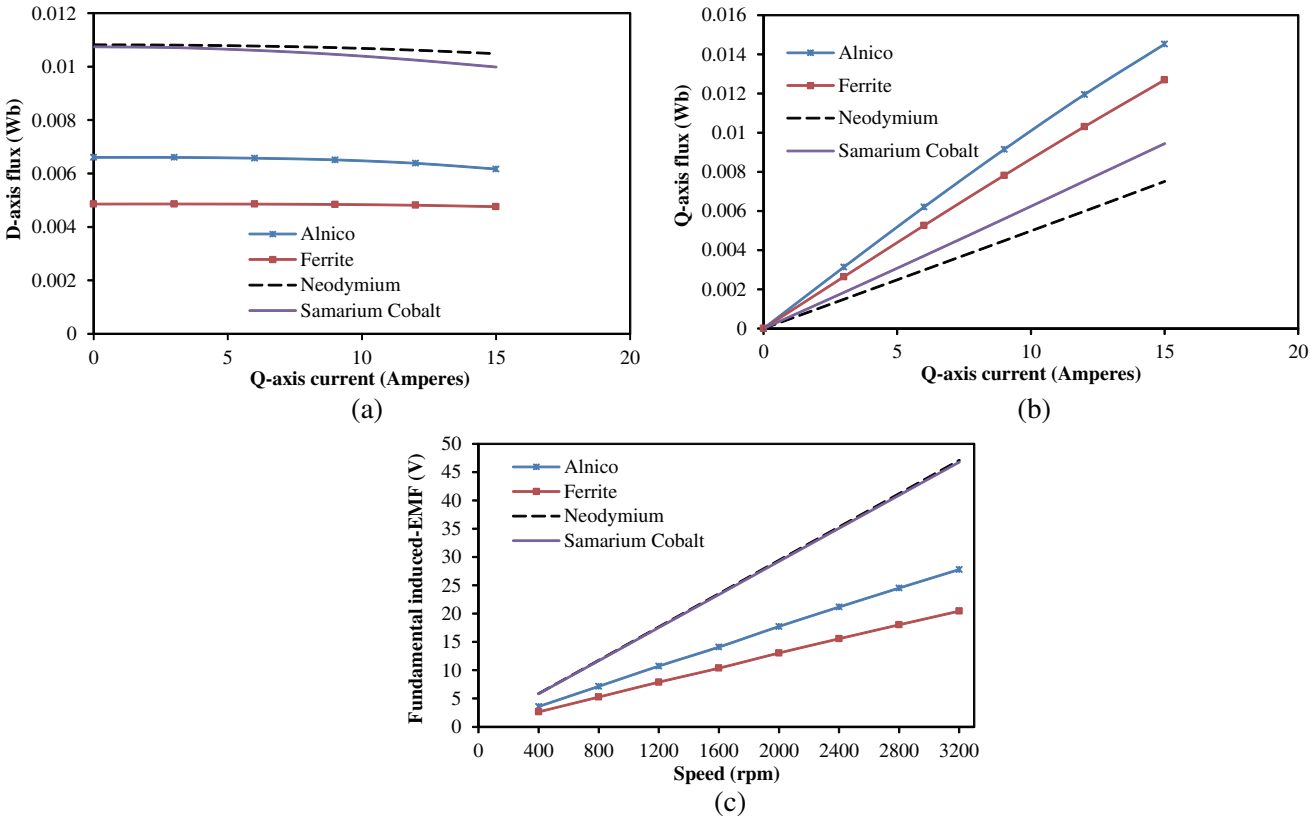

Figure 6. 2D FEA comparison of axes flux and induced-EMF, 400 rev/min, (a) D-axis versus current, (b) Q-axis versus current, (c) induced-EMF versus speed.

observed that the D-axis flux variation of the investigated machine is insensitive to the injected low quadrature-axis currents; however, it would be negatively affected as the current level increases due to the impact of armature reaction. Similarly, it is observed from Fig. 6(b) that there is a linear relationship between Q-axis flux and the corresponding Q-axis current. Meanwhile, there is a direct proportionality between the induced-electromotive force magnitude and operating speed of the machine, as depicted in Fig. 6(c). The output torque waveforms of the compared magnets at different load settings are shown in Fig. 7(a). Obviously, the obtained torque performance is dependent on both the used magnetic material and the injected current. The most promising candidates amongst all are the machines that are provided with rare-earth magnets, in particular, the neodymium type, though with larger ripple in consonant with their high cogging torque amplitudes.

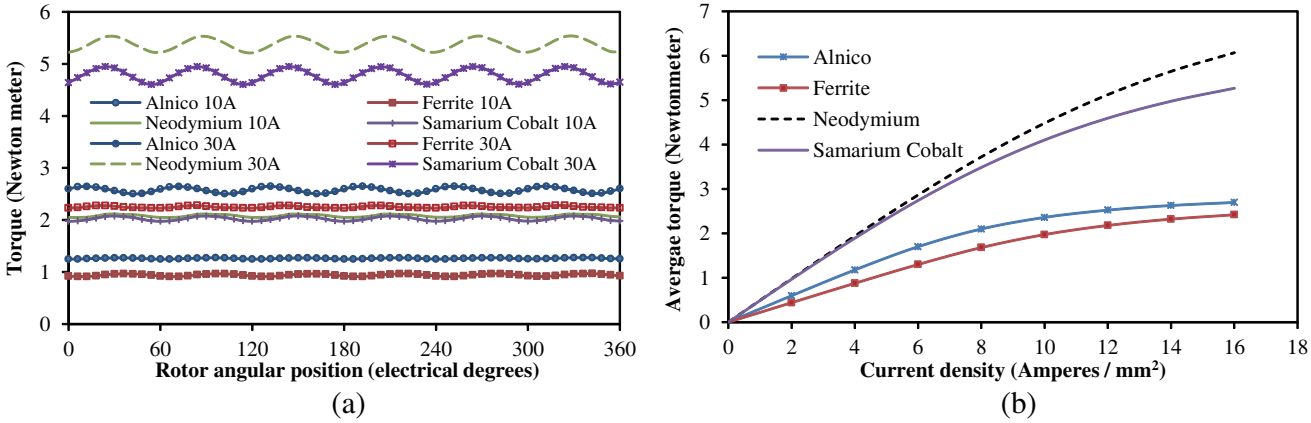

Figure 7. 2D FEA comparison of electromagnetic and average torque. (a) torque versus rotor position, (b) torque versus current density.

However, Fig. 7(b) reveals that the machine having ferrite and alnico material would undergo quicker saturation under heavy electromagnetic loading, owing to its low amount of coercivity, in addition to its low energy products compared to the machine that has either neodymium or samarium-cobalt as its magnetic material. Moreover, the inherent high inductance values of the non-rare-earth PMs would also aggravate its saturation level.

3. UNBALANCED MAGNETIC PULL (UMP) CHARACTERISTICS

The variation of rotor unbalanced magnetic pull (UMP), which is also known as unbalanced magnetic force is displayed in Figs. 8 and 9. It could be observed that the resultant magnitude of this pull is larger in the machines having rare-earth magnetic materials. The predicted 2D FEA and 3D FEA UMP values of the analyzed machine types are quantitatively compared in Table 2. Further, the vertical and horizontal components of these forces show that the use of rare-earth magnet would result in larger UMP axis values, as illustrated in Fig. 9. The recorded high amounts of UMP on the rare-earth types would require a systematic reduction through design/optimization techniques, in order to avoid possible noise and vibration in the machine.

The UMP horizontal and vertical elements are calculated using Eqs. (5) and (6), respectively.

$$P_x = \frac{Rl}{2\mu_o} \int_0^{2\pi} \left[\left(B_\alpha^2 - B_R^2 \right) \cos\alpha + 2 B_R B_\alpha \sin\alpha \right] \Delta\alpha \tag{5}$$

$$P_y = \frac{Rl}{2\mu_o} \int_0^{2\pi} \left[\left(B_\alpha^2 - B_R^2 \right) \sin\alpha - 2 B_R B_\alpha \cos\alpha \right] \Delta\alpha \tag{6}$$

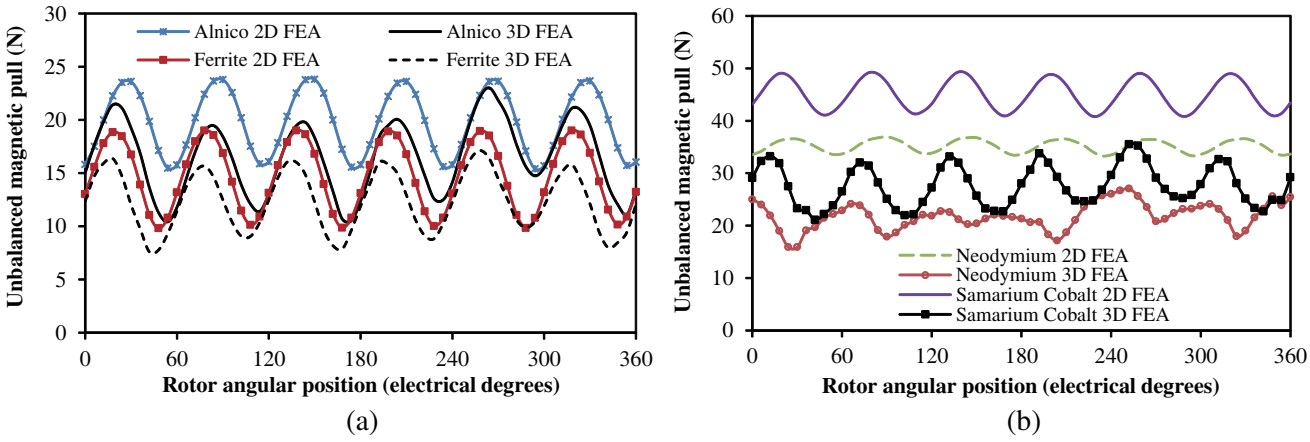

Figure 8. Comparison of unbalanced magnetic pull at 15 A, (a) non-rare-earth, (b) rare-earth.

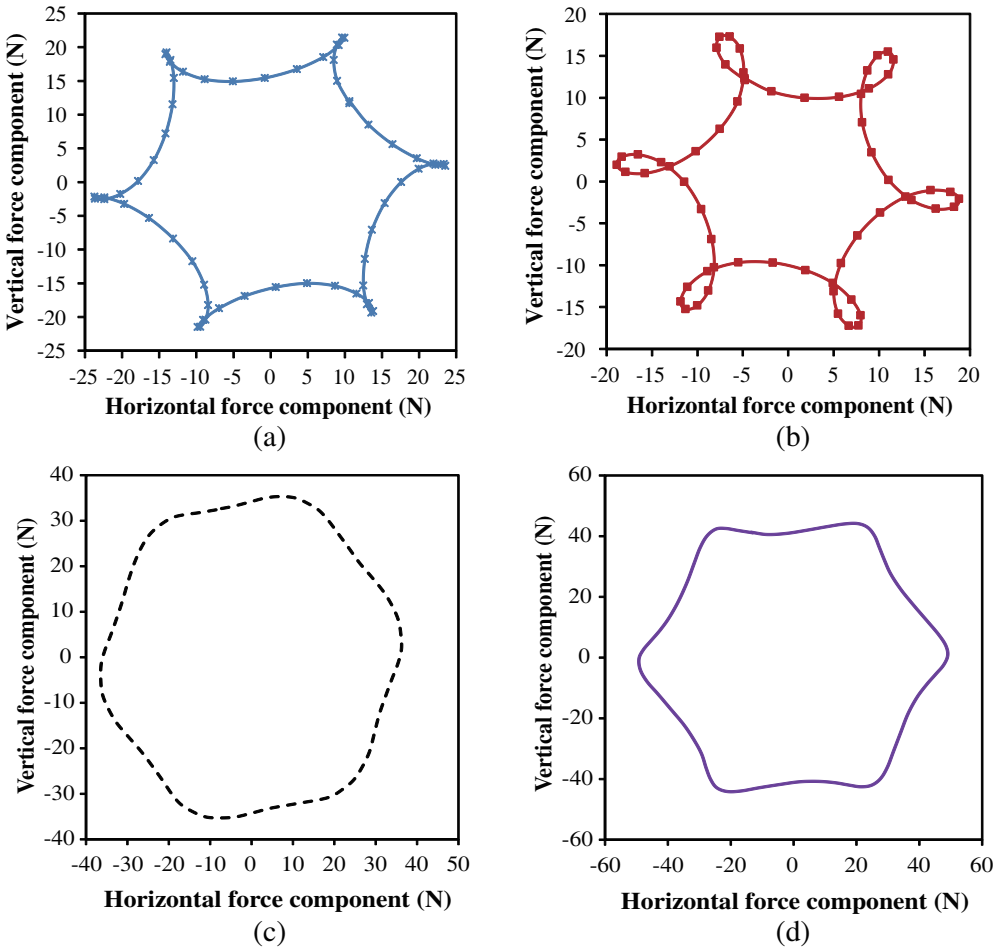

Figure 9. 2D FEA comparison of UMP in different directions, (a) alnico, (b) ferrite, (c) neodymium, (d) samarium.

where P_x and P_y are the horizontal and vertical pull elements on the rotor; l is the machine stack length; R is the airgap radius; B_R and B_α are the airgap flux-density in centrifugal and perimetric directions [20].

4. INDUCTANCE CHARACTERISTICS

The self-inductance and mutual-inductance of the compared machine types are shown in Fig. 10. The largest amount of self-inductance is observed in the alnico-made machine, followed by its complementing ferrite-type, while the least value of self-inductance is obtained from the neodymium-type of machine. This implies that the non-rare-earth magnets would have greater capability to withstand short-circuit faults, since the primary requirement to overcome such faults is possession of high self-inductance value, as proved in [21]. Nevertheless, the comparison of mutual inductance presented in Figs. 10(c) and (d) shows that the rare-earth magnets have lower mutual-inductance than the non-rare-earth counterparts. It is worth noting that the compared machines have negative mutual inductance values, implying that its actual coil current directions should have been the reversed polarities. More so, the predicted ratio of mutual-inductance to self-inductance listed in Table 2 reveals that lower value of the inductance ratios, which are paramount for effective fault-tolerance capacity, is obtainable in the rare-earth PMs; these results are supported by the long-established fault-tolerance concept detailed in [22] and reemphasized in [23].

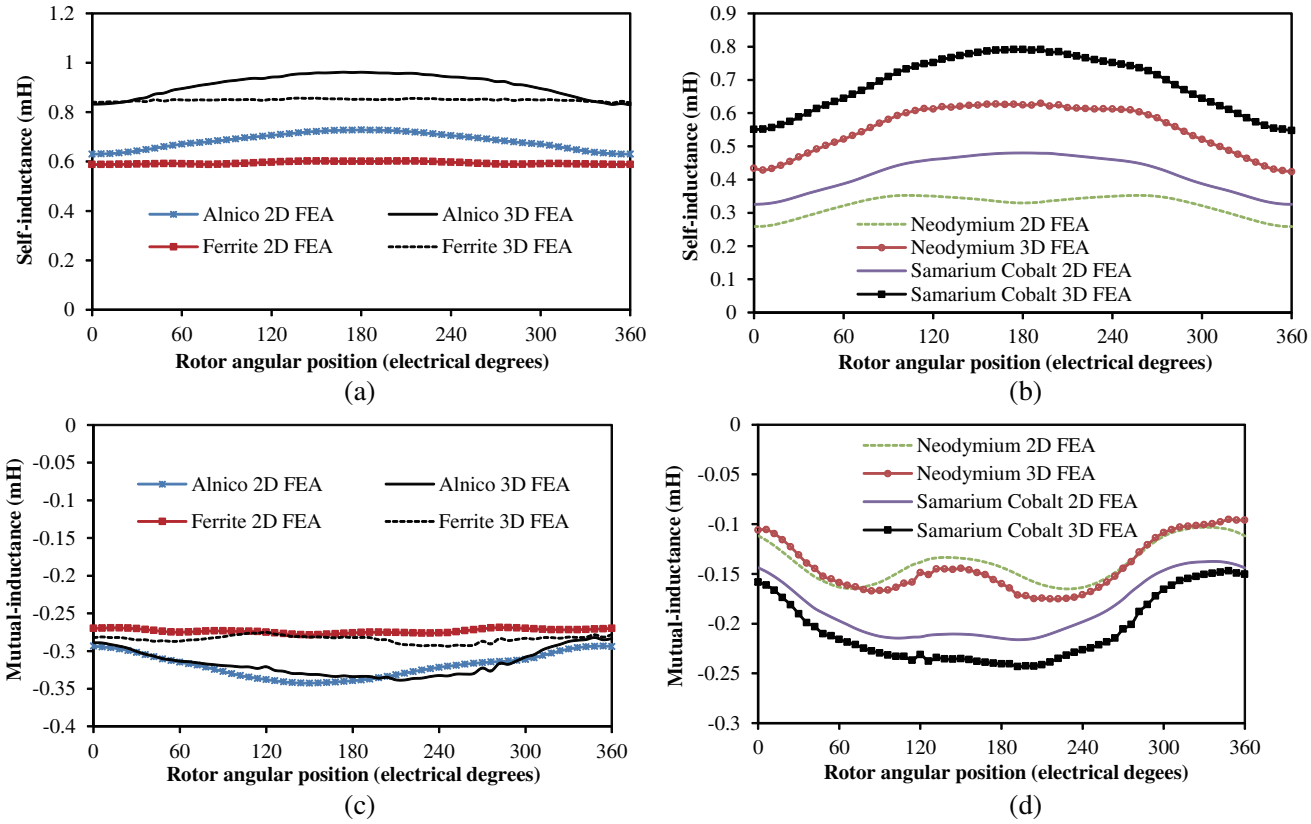

Figure 10. 2D and 3D FEA inductance variation with rotor position, (a) non-rare-earth self-inductance, (b) rare-earth self-inductance, (c) non-rare-earth mutual-inductance, (d) rare-earth mutual-inductance.

The computed self-inductance and mutual-inductance are obtained using Eqs. (7) and (8). More so, the 2D FEA and 3D FEA computed values are compared in Table 2. The noticeable differences between the predicted 2D FEA and 3D FEA inductance results are due to the impact of end windings as well as the small ratio of machine's stack length to machine diameter.

$$L_{AA} = \frac{\Psi_A(I_A = I, I_B = I_C = 0) - \Psi_A(I_A = I_B = I_C = 0)}{I_A} \tag{7}$$

$$M_{AB} = \frac{\Psi_B(I_A = I, I_B = I_C = 0) - \Psi_B(I_A = I_B = I_C = 0)}{I_A} \tag{8}$$

Table 2. Comparison of 2D FEA and 3D FEA results.

Item	Value							
Material type/grade	**Alnico (A500)**	**Ferrite (F5)**	**NdFeB (N52)**	**SmCo (S24)**	**Alnico (A500)**	**Ferrite (F5)**	**NdFeB (N52)**	**SmCo (S24)**
Finite Element Analysis	**2D FEA**				**3D FEA**			
Maximum cogging torque (Nm)	0.0047	0.0059	0.0223	0.0290	0.0333	0.0170	0.1748	0.0912
Cogging torque FFT (Nm)	0.0043	0.0051	0.0134	0.0254	0.0142	0.0083	0.1044	0.0473
Maximum force, UMP (N)	23.82	18.99	33.08	41.89	23.01	17.12	27.05	35.51
Average force, UMP (N)	19.77	14.68	31.11	35.17	16.46	12.35	21.87	27.64
Peak self-inductance, (mH)	0.7280	0.6017	0.3526	0.4803	0.9620	0.8570	0.6291	0.7914
Av. self-inductance, L_{AA} (mH)	0.6836	0.5942	0.3222	0.4167	0.9102	0.8494	0.5530	0.6888
Peak mutual-inductance, (mH)	−0.29	−0.27	−0.10	−0.14	−0.28	−0.28	−0.10	−0.15
Av. Mutual-inductance, M_{AB} (mH)	−0.32	−0.27	−0.14	−0.1854	−0.32	−0.28	−0.14	−0.21
Absolute ratio of M_{AB} to L_{AA} (%)	46.81	45.44	43.45	44.49	35.16	32.96	25.32	30.49

where L_{AA} is the self-inductance of Phase A, M_{AB} the mutual-inductance between Phases A and B, I_A the magnitude of supplied current, and Ψ_A and Ψ_B are the open-circuit flux-linkages contributed simultaneously by the PMs and conductors in the relevant Phases.

The variations of both direct-axis and quadrature-axis inductances with rotor angular positions are presented in Fig. 11. It is shown that machine's windings inductances have more or less similar values in the two axes, which imply that they would have negligible reluctance torque and consequently, saliency ratio almost approximately 1, as itemized in Table 1. Meanwhile, the largest axis inductance is obtained from the alnico-made machine, followed by its ferrite-equivalent, while the least axis inductance is shown in the neodymium-equipped machine. More so, the results of Fig. 11 imply that there is an inverse proportionality between the amount of coercivity of the magnets and the resulting axis inductances. Moreover, the larger the winding inductance value is, the lower its saturation withstand ability is, since saturation effect is synonymous to the level of winding inductance [13] in the system. Thus, the neodymium-magnet would have the greatest potential to withstand magnetic saturation and vice-versa. Similarly, the direct- and quadrature-axis inductances are predicted using Eqs. (9) and (10).

$$L_D = \frac{\Psi_D(I_d = -I_d, I_q = 0) - \Psi_D(I_d = I_q = 0)}{I_d} \tag{9}$$

$$L_Q = \frac{\Psi_Q(I_q = I_q, I_d = 0) - \Psi_Q(I_d = I_q = 0)}{I_q} \tag{10}$$

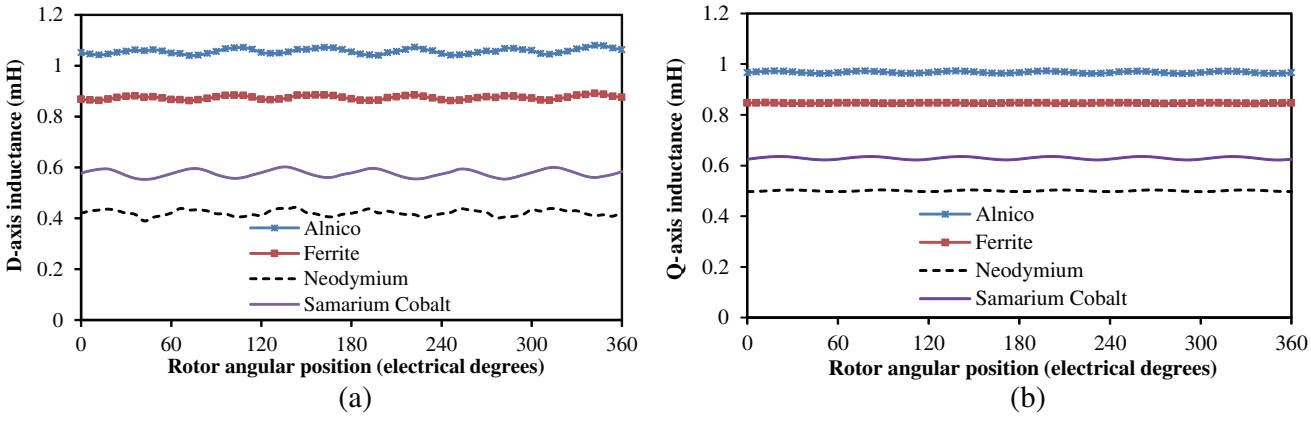

Figure 11. 2D FEA inductance comparison at Q-axis current of 15 A. (a) D-axis, (b) Q-axis.

where L_D and L_Q are the direct-axis and quadrature-axis inductance; I_d and I_q are the direct-axis and quadrature-axis current; Ψ_D and Ψ_Q are the direct-axis and quadrature-axis flux-linkage.

It should be noted that the Q-axis inductances are slightly larger than their corresponding D-axis equivalents in machines having rare-earth magnets while the reverse is the case in their non-rare-earth counterparts, owing to the great discrepancies in their coercivity and magnetic remanence profiles. Consequently, the low amount of D-axis inductance in the rare-earth magnets would adversely affect its field-weakening potential as reported in [24]; this claim is supported and enumerated in Table 1. The flux-weakening potential F_{wp} of the investigated flux-switching PM machine is evaluated using Eq. (11). The desired flux-weakening proficiencies of permanent magnet machines as well as resulting wide speed range could be realized through adequate reduction of the generated flux via a flux leakage path with a controllable Q-axis current operation, coupled with adequate manipulation of the machine's axis inductances, as established in [25] and [26].

$$F_{wp} = \frac{L_D I}{\Psi_{PM}} \tag{11}$$

where Ψ_{PM} is the flux-linkage due to magnet, and I is the rated current [24].

Furthermore, loss outlines of the compared machine types in one electric period, under varying rotor angular positions are depicted in Fig. 12. It is revealed that the ferrite- and alnico-made machines have very negligible low eddy current loss from the magnets, as seen in Fig. 12(a), as a result of its very high resistivity contents. Nevertheless, these two mentioned machine topologies exhibit larger amount of total core loss on the average than their equivalent rare-earth magnet counterparts, as shown in Fig. 12(b). Moreover, the finite element predicted efficiency values of the compared machine types having alnico, ferrite, neodymium, and samarium materials, at rated current and speed conditions are: 79.83%, 75.76%, 87.22%, and 86.58%, respectively. Similarly, the generated electromagnetic output power of the compared machine types at the operating base speed is: 206.57 Watts, 186.57 Watts, 449.67 Watts, and 396.40 Watts, respectively. Thus, the rare-earth machine configurations are more promising in terms of better efficiency and output electromagnetic power than their non-rare-earth equivalents. More so, core loss magnitudes of electrical machines could be reduced with a corresponding increase in efficiency by implementing a soft magnetic material on the cores or by using other materials with low-loss contents such as alloy of nickel and iron, though with high permeability values.

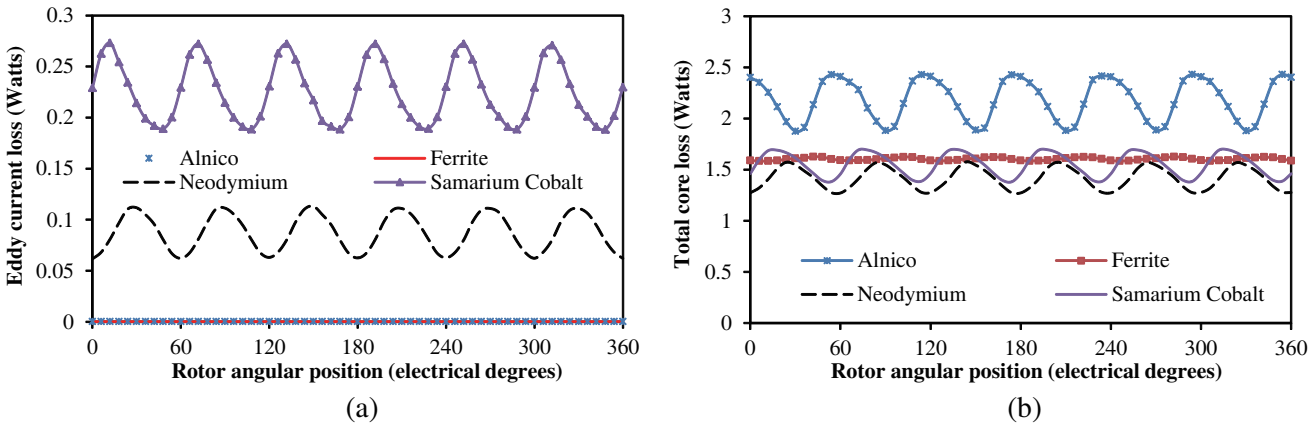

Figure 12. 2D FEA loss comparison at 15 Amperes, 400 rpm. (a) Magnet eddy current loss. (b) Total core loss.

However, remarkable electromagnetic output could be realized from a given electric machine by adopting improved magnetic materials developed through technological advancement, as noted in [16] and [2]. Also, significant impact of applying improved magnetic material to achieve higher electromagnetic performance ranging from enhanced output power, torque, efficiency, low loss, and reduced weight to low cost cannot be overestimated.

5. CONCLUSION

The effect of permanent magnet remanence and coercive force or coercivity on the output performance of permanent magnet machine is presented. The investigation shows that the machines equipped with rare-earth magnetic materials have higher UMP and cogging torque, albeit, with better air-gap flux-density/magnetic remanence and superior torque competence compared to the ones with non-rare-earth magnetic materials. In addition, the rare-earth magnetic machines would have better ability to withstand saturation effects due to its possession of lower winding inductance values. Moreover, the outcome of the mutual-inductance to self-inductance ratio reveals that the machines having rare-earth magnets would exhibit greater fault-tolerant ability than the non-rare-earth ones. More so, the results also reveal that the investigated rare-earth magnet machine topologies exhibit improved efficiency and enhanced electromagnetic output power compared to their non-rare-earth counterparts. The analyzed machine could be implemented in traction and automobile uses for high torque direct-drive applications. Comparative analysis of the impacts of end winding on the analyzed machine parameters is also presented and quantitatively compared with the 2D FEA predictions. Above all, the rare-earth magnetic machines produced both the largest electromagnetic output power and efficiency.

REFERENCES

1. Morimoto, S., S. Ooi, Y. Inoue, and M. Sanada, "Experimental evaluation of a rare-earth-free PMASynRM with ferrite magnets for automotive applications," *IEEE Transactions on Industrial Electronics*, Vol. 61, No. 10, 5749–5756, 2014, doi: 10.1109/TIE.2013.2289856.
2. Ramesh, P. and N. C. Lenin, "High power density electrical machines for electric vehicles—comprehensive review based on material technology," *IEEE Transactions on Magnetics*, Vol. 55, No. 11, 1–21, 2019, doi: 10.1109/TMAG.2019.2929145.
3. Bonthu, S. S. R., A. Arafat, and S. Choi, "Comparisons of rare-earth and rare-earth free external rotor permanent magnet assisted synchronous reluctance motors," *IEEE Transactions on Industrial Electronics*, Vol. 64, No. 12, 9729–9738, 2017, doi: 10.1109/TIE.2017.2711580.
4. Yu, D., X. Huang, X. Zhang, J. Zhang, Q. Lu, and Y. Fang, "Optimal design of outer rotor interior permanent magnet synchronous machine with hybrid permanent magnet," *IEEE Transactions Applied Superconductivity*, Vol. 29, No. 2, 1–5, 2019, doi: 10.1109/TASC.2019.2895260.
5. Wu, W., X. Zhu, L. Quan, Y. Du, Z. Xiang, and X. Zhu, "Design and analysis of a hybrid permanent magnet assisted synchronous reluctance motor considering magnetic saliency and PM usage," *IEEE Transactions on Applied Superconductivity*, Vol. 28, No. 3, 1–6, 2018, doi: 10.1109/TASC.2017.2775584.
6. Chen, Y., T. Cai, X. Zhu, D. Fan, and Q. Wang, "Analysis and design of a new type of less-rare-earth hybrid-magnet motor with different rotor topologies," *IEEE Transactions on Applied Superconductivity*, Vol. 30, No. 4, 1–6, 2020, doi: 10.1109/TASC.2020.2965879.
7. Chen, J. T., Z. Q. Zhu, S. Iwasaki, and R. P. Deodhar, "Influence of slot opening on optimal stator and rotor pole combination and electromagnetic performance of switched-flux PM brushless AC machines," *IEEE Transactions on Industry Applications*, Vol. 47, No. 4, 1681–1691, 2011, doi: 10.1109/TIA.2011.2155011.
8. Petrov, I., M. Niemela, P. Ponomarev, and J. Pyrhonen, "Rotor surface ferrite permanent magnets in electrical machines: advantages and limitations," *IEEE Transactions on Industrial Electronics*, Vol. 64, No. 7, 5314–5322, 2017, doi: 10.1109/TIE.2017.2677320.
9. Vartanian, R., H. A. Toliyat, B. Akin, and R. Poley, "Power factor improvement of synchronous reluctance motors, SynRM) using permanent magnets for drive size reduction," *Proceedings of Annual IEEE Applied Power Electronics Conference and Exposition, APEC)*, 628–633, Orlando, USA, 2012, doi: 10.1109/APEC.2012.6165884.
10. Zhao, W., D. Chen, T. A. Lipo, and B. I. Kwon, "Performance improvement of ferrite-assisted synchronous reluctance machines using asymmetrical rotor configurations," *IEEE Transactions on Magnetics*, Vol. 51, No. 11, 1–4, 2015, doi: 10.1109/TMAG.2015.2436414.

11. Jung, Y. H., M. R. Park, K. O. Kim, J. W. Chin, J. P. Hong, and M. S. Lim, "Design of high-speed multilayer IPMSM using ferrite PM for EV traction considering mechanical and electrical characteristics," *IEEE Transactions on Industry Applications*, Vol. 57, No. 1, 327–339, 2021, doi: 10.1109/TIA.2020.3033783.
12. Huang, H., Y. S. Hu, Y. Xiao, and H. Lyu, "Research of parameters and antidemagnetization of rare-earth-less permanent magnet-assisted synchronous reluctance motor," *IEEE Transactions on Magnetics*, Vol. 51, No. 11, 1–4, 2015, doi: 10.1109/TMAG.2015.2445934.
13. Zhu, X., S. Yang, Y. Du, Z. Xiang, and L. Xu, "Electromagnetic performance analysis and verification of a new flux-intensifying permanent magnet brushless motor with two-layer segmented permanent magnets," *IEEE Transactions on Magnetics*, Vol. 52, No. 7, 1–4, 2016, doi: 10.1109/TMAG.2016.2519465.
14. Kim, K. H., H. I. Park, S. M. Jang, D. J. You, and J. Y. Choi, "Comparative study of electromagnetic performance of high-speed synchronous motors with rare-earth and ferrite permanent magnets," *IEEE Transactions on Magnetics*, Vol. 52, No. 7, 1–4, 2016, doi: 10.1109/TMAG.2016.2532901.
15. Awah., C. C., "Effect of permanent magnet material on the electromagnetic performance of switched-flux permanent magnet machine," *Electrical Engineering*, Vol. 103, No. 3, 1647–1660, 2021, doi: https://doi.org/10.1007/s00202-020-01155-8.
16. El-Refaie, A., "Role of advanced materials in electrical machines," *CES Transactions on Electrical Machines and Systems*, Vol. 3, No. 2, 124–132, 2019, doi:10.30941/CESTEMS.2019.00018.
17. Tahanian, H., M. Aliahmadi, and J. Faiz, "Ferrite permanent magnets in electrical machines: opportunities and challenges of a non-rare-earth alternative," *IEEE Transactions on Magnetics*, Vol. 56, No. 3, 1–20, 2020, doi: 10.1109/TMAG.2019.2957468.
18. Xu, H., J. Li, J. Chen, Y. Lu, and M. Ge, "Analysis of a hybrid permanent magnet variable-flux machine for electric vehicle tractions considering magnetizing and demagnetizing current," *IEEE Transactions on Industry Applications*, Vol. 57, No. 6, 5983–5992, 2021, doi: 10.1109/TIA.2021.3115077.
19. Liu, X., H. Chen, J. Zhao, and A. Belahcen, "Research on the performances and parameters of interior PMSM used for electric vehicles," *IEEE Transactions on Industrial Electronics*, Vol. 63, No. 6, 3533–3545, 2016, doi: 10.1109/TIE.2016.2524415.
20. Zhu, Z. Q., D. Ishak, D. Howe, and J. Chen, "Unbalanced magnetic forces in permanent-magnet brushless machines with diametrically asymmetric phase windings," *IEEE Transactions on Industry Applications*, Vol. 43, No. 6, 1544–1553, 2007, doi: 10.1109/IAS.2005.1518484.
21. Barcaro, M., N. Bianchi, and F. Magnussen, "Six-Phase supply feasibility using a PM fractional-slot dual winding machine," *IEEE Transactions on Industry Applications*, Vol. 47, No. 5, 2042–2050, 2011, doi: 10.1109/TIA.2011.2161859.
22. Thomas, A. S., Z. Q. Zhu, R. L. Owen, G. W. Jewell, and D. Howe, "Multiphase flux-switching permanent-magnet brushless machine for aerospace application," *IEEE Transactions on Industry Applications*, Vol. 45, No. 6, 1971–1981, 2009, doi: 10.1109/TIA.2009.2031901.
23. Kang, M., L. Xu, J. Ji, and X. Zhu, "Design and analysis of a high torque density hybrid permanent magnet excited vernier machine," *Energies*, Vol. 15, No. 5, 1723, 2022, https://doi.org/10.3390/en15051723.
24. Hua, W. and C. Ming, "Inductance characteristics of 3-phase flux-switching permanent magnet machine with doubly-salient structure," *Proceedings of IEEE International Conference on Power Electronics and Motion Control*, 1–5, Shanghai, China, 2006, doi: 10.1109/IPEMC.2006.4778302.
25. Liu, X., G. Guo, L. Du, and W. Zhu, "Multi-objective optimal design and analysis of variable leakage flux IPM motors for improve flux-weakening ability," *Progress In Electromagnetics Research C*, Vol. 113, 147–160, 2021, doi:10.2528/PIERC21042502.
26. Liu, X., G. Guo, S. Zhu, and J. Liang, "Design and analysis of variable leakage flux flux-intensifying motor for improve flux-weakening ability," *Progress In Electromagnetics Research M*, Vol. 103, 221–233, 2021, doi:10.2528/PIERM21070204.